Inorganic Chemistry

Article

pubs.acs.org/IC

Bonding Trends Traversing the Tetravalent Actinide Series: Synthesis, Structural, and Computational Analysis of $An^{IV}(^{Ar}acnac)_4$ Complexes (An = Th, U, Np, Pu; $^{Ar}acnac$ = Ar*N*C(Ph)CHC(Ph)*O*; Ar = 3,5-$^{t}Bu_2C_6H_3$)

David D. Schnaars,[†,‡] Andrew J. Gaunt,*[,‡] Trevor W. Hayton,*[,†] Matthew B. Jones,[‡] Ian Kirker,[∥] Nikolas Kaltsoyannis,*[,∥] Iain May,[‡] Sean D. Reilly,[‡] Brian L. Scott,[§] and Guang Wu[†]

[†]Department of Chemistry and Biochemistry, University of California Santa Barbara, Santa Barbara, California 93106, United States

[‡]Chemistry Division, and [§]Materials Physics and Applications Division, Los Alamos National Laboratory, Los Alamos, New Mexico 87545, United States

[∥]Department of Chemistry, University College London, 20 Gordon Street, London WC1H 0AJ, United Kingdom

Supporting Information

ABSTRACT: A series of tetravalent An(IV) complexes with a bis-phenyl β-ketoiminate N,O donor ligand has been synthesized with the aim of identifying bonding trends and changes across the actinide series. The neutral molecules are homoleptic with the formula $An(^{Ar}acnac)_4$ (An = Th (**1**), U (**2**), Np (**3**), Pu (**4**); $^{Ar}acnac$ = Ar*N*C(Ph)CHC(Ph)*O*; Ar = 3,5-$^{t}Bu_2C_6H_3$) and were synthesized through salt metathesis reactions with actinide chloride precursors. NMR and electronic absorption spectroscopy confirm the purity of all four new compounds and demonstrate stability in both solution and the solid state. The Th, U, and Pu complexes were structurally elucidated by single-crystal X-ray diffraction and shown to be isostructural in space group *C*2/*c*. Analysis of the bond lengths reveals shortening of the An−O and An−N distances arising from the actinide contraction upon moving from **1** to **2**. The shortening is more pronounced upon moving from **2** to **4**, and the steric constraints of the tetrakis complexes appear to prevent the enhanced U−O versus Pu−O orbital interactions previously observed in the comparison of $UI_2(^{Ar}acnac)_2$ and $PuI_2(^{Ar}acnac)_2$ bis-complexes. Computational analysis of models for **1**, **2**, and **4** (**1a**, **2a**, and **4a**, respectively) concludes that both the An−O and the An−N bonds are predominantly ionic for all three molecules, with the An−O bonds being slightly more covalent. Molecular orbital energy level diagrams indicate the largest 5f-ligand orbital mixing for **4a** (Pu), but spatial overlap considerations do not lead to the conclusion that this implies significantly greater covalency in the Pu−ligand bonding. QTAIM bond critical point data suggest that both U−O/U−N and Pu−O/Pu−N are marginally more covalent than the Th analogues.

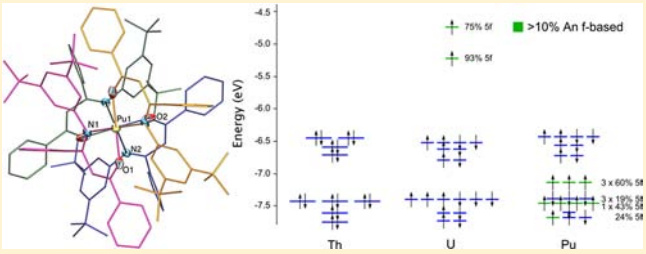

INTRODUCTION

Actinide chemistry is central to numerous nuclear fuel cycle applications, such as separations for used fuel processing, legacy waste remediation, and environmental mobility prediction/mitigation.[1,2] Unfortunately, the knowledge and understanding of fundamental actinide bonding trends and coordination modes significantly lags behind that of other elemental series in the periodic table. In terms of the actinide series, there have been far fewer studies into molecular transuranic compounds than have been reported for uranium or thorium.[1,3,4] These understudied elements represent a significant knowledge gap because several transuranic radioisotopes pose some of the most difficult separation challenges and waste toxicity concerns that arise from the storage, treatment, and eventual disposal of used nuclear fuel.[2,5] The lack of actinide studies that encompass transuranic molecules also places limitations on our grasp of bonding and electronic structure trends across the 5f series, and how both subtle and major changes in ligand binding may impact the behavior of the different actinide ions in terms of speciation and separation selectivity. In this respect, a topic greatly debated in the literature is the role that subtle differences in covalent interactions play in influencing An(III)/Ln(III) separations achieved by certain ligands containing soft donor atoms (primarily N and S).[6−12] Moreover, it is not just An(III)/Ln(III) separation schemes that are of interest, but novel methods are under consideration for the chemical control of uranium, neptunium, and plutonium as well.[2,13] Advances in early actinide processing capabilities can only be rationally developed and optimized through an underlying comprehension of subtle changes in chemistry and bonding of all of the

Received: May 29, 2012
Published: July 26, 2012

   dx.doi.org/10.1021/ic301109f | *Inorg. Chem.* 2012, 51, 8557−8566

relevant actinide ions with a wide range of ligand types and donor atoms.

In light of these knowledge deficiencies, we are interested in comparing the metrical parameters of structurally similar f-element molecules containing different metal centers. We also apply a combined experimental and computational approach with the aim of providing DFT calculation results that model experimental data and help to offer an electronic structure basis to explain bonding differences. We believe that utilizing both experiment and theory in synergy provides more convincing conclusions than either applied in a stand-alone fashion. However, even with this combined methodology, it is important to recognize the difficulty in attributing small bonding differences to covalency changes conclusively, and this complexity is probably part of the reason why the topic of covalency in actinide molecules is still of great interest despite being discussed since the 1950s.[14,15]

The majority of comparative "covalency studies" have focused upon An(III) versus Ln(III) bonding comparisons.[16] Recently, we have turned our attention toward studying bonding changes within the tetravalent An(IV) series. There are very few reports of isostructural molecular An(IV) systems with full single-crystal structural determination for anything other than U(IV) versus Th(IV), which are both weakly radioactive and can be handled without specialist radiological facilities. Nonetheless, a few comparisons that include, but also stretch beyond Th and U, have been reported. Sokolova et al. isolated and structurally characterized the complexes $[An(\alpha_2\text{-}P_2W_{17}O_{61})_2]^{16-}$ (An = Th, U, Np, Pu, Am) in which the An−O distances followed those expected from the actinide contraction with ionic bonding being the only significant influence.[17] There are also a few examples of structurally similar series of $[AnCl_6]^{2-}$ An(IV) dianionic complexes.[18]

In 2011, we communicated the comparison of U(IV) and Pu(IV) complexes with an N,O donor β-ketoiminate ligand (^{Ar}acnac, Figure 1).[19] Given our previous studies with soft

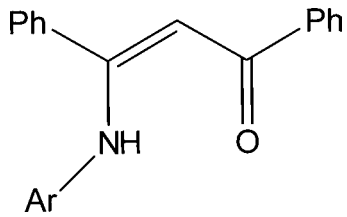

Figure 1. The ^{Ar}acnac N,O donor ligand (Ar = 3,5-^{t}Bu$_2$C$_6$H$_3$), shown with the nitrogen atom protonated.

donor ligands,[16] we had anticipated that if any covalency differences were to be inferred from bond length comparisons between the $UI_2(^{Ar}acnac)_2$ and $PuI_2(^{Ar}acnac)_2$ molecules, then they would be in the M−L bonds to the relatively soft nitrogen atom rather than the hard oxygen donor atom. Surprisingly, while the An−N bonds appeared to follow the actinide contraction consistent with ionic interactions strengthening from U(IV) to Pu(IV), an unexpectedly short U−O bond was found and attributed to enhanced orbital overlap interactions in the U−O versus Pu−O bonding. Attaining a better understanding of these bonding differences may have implications for how they can be exploited in the design of more robust ligand systems for actinide separation technologies.

In this article, we report a new series of An(IV) complexes with the ^{Ar}acnac N,O donor ligand, the $An(^{Ar}acnac)_4$ (An = Th (**1**), U (**2**), Np (**3**), Pu (**4**)) molecules. X-ray structural determinations are presented for three of the homoleptic tetrakis-complexes (Th, U, Pu) along with computational modeling.

RESULTS AND DISCUSSION

Addition of 4 equiv of Na(^{Ar}acnac), prepared in situ from the protonated form of the ligand and Na[N(SiMe$_3$)$_2$] base, to an Et$_2$O suspension of ThCl$_4$(DME)$_2$ results in the formation of a yellow solution, from which Th(^{Ar}acnac)$_4$ (**1**) can be isolated as a yellow microcrystalline solid in 68% yield (Scheme 1). The

Scheme 1. Synthesis of Complexes 1−4

$$AnCl_4(DME)_n \xrightarrow[-\ 4\ NaCl]{4\ Na^{Ar}acnac} An(^{Ar}acnac)_4 \xleftarrow[-\ 2\ [PPh_4][Cl]\ -\ 4\ NaCl]{4\ Na^{Ar}acnac} [PPh_4]_2[AnCl_6]$$

An = Th, n = 2, **1**; U, n = 0, **2** | Ar = 3,5 ^{t}Bu$_2$C$_6$H$_3$ | An = Np, **3**; Pu, **4**

uranium analogue, U(^{Ar}acnac)$_4$ (**2**), can be synthesized similarly from UCl$_4$, resulting in the isolation of **2** as a burnt-orange microcrystalline solid in a 64% yield (Scheme 1). Formation of the analogous transuranic complexes An(^{Ar}acnac)$_4$, where An = Np (**3**) and Pu (**4**), can be accomplished through addition of 4 equiv of Na(^{Ar}acnac) to the respective $[PPh_4]_2[AnCl_6]$ starting materials,[18] resulting in a crystalline orange solid of Np(^{Ar}acnac)$_4$ and crystalline red solid of Pu(^{Ar}acnac)$_4$ in 47% and 59% yields, respectively. Complex **4** can also be formed by reaction of $[PPh_4]_2[PuCl_6]$ with only 2 equiv of Na(^{Ar}acnac).[19] Under these conditions, 0.5 equiv of $[PPh_4]_2[PuCl_6]$ remains unreacted. The preferred formation of **4** over the putative PuCl$_2$(^{Ar}acnac)$_2$ is likely due to the fact that $[PPh_4]_2[PuCl_6]$ is poorly soluble in THF, which results in a large effective local excess of ^{Ar}acnac ligand relative to Pu(IV) ions in the reaction solution even when only 2 equiv of ligand is present.

Complexes **1**−**4** are soluble in THF, Et$_2$O, CH$_2$Cl$_2$, DME, toluene, hexanes, and *n*-pentane, but are not soluble in CH$_3$CN or DMF. NMR spectra of **1**−**4** are shown in Figures S9−S16. The ^{1}H NMR spectrum of **1** in CD$_2$Cl$_2$ is consistent with a diamagnetic Th(IV) complex and displays two large resonances at 0.87 and 0.70 ppm. These resonances, each integrating for 36 protons, are attributed to the ^{t}Bu substituents on the N-aryl group, which are inequivalent due to a sterically induced lack of rotation about the N−C$_{ipso}$ bond. A corresponding set of ^{t}Bu resonances is also observed in the ^{1}H NMR spectra for complexes **2** (3.61 and −2.76 ppm), **3** (0.75 and 0.38 ppm), and **4** (1.89 and −0.26 ppm), indicating that rotation of the bulky aryl group is restricted in each case. The inequivalent ^{t}Bu groups provide a facile method by which to distinguish the tetrakis-complexes in solution from the previously reported $AnX_2(^{Ar}acnac)_2$ (An = U, X = Cl or I; An = Pu, X = I) bis-complexes, for which the ^{t}Bu groups are identical by symmetry and also free to rotate about the N−C$_{ipso}$ bond, resulting in their equivalence in the ^{1}H NMR spectrum.[19] We have also previously observed sterically restricted rotation about the N−C$_{ipso}$ bond of the ^{Ar}acnac ligand in complexes with sterically bulky coligands such as $U(OSiPh_3)(OB\{C_6F_5\}_3)(^{Ar}acnac)_2$ and $U(OSiEt_3)(OB\{C_6F_5\}_3)(^{Ar}acnac)_2$.[20,21]

Turning to electronic absorption spectroscopy of **2**−**4** in the UV/vis/nIR region, multiple bands are observed arising from charge-transfer, 5f−6d, and 5f−5f transitions. Optical spectra of An(IV) ions, both in solid compounds and ions in solution, have been the subject of much study and interpretation.[22−28]

dx.doi.org/10.1021/ic301109f | Inorg. Chem. 2012, 51, 8557−8566

The spectra are extremely complicated (due to spin−orbit coupling and ligand field effects), and one cannot readily transfer a set of electronic transition assignments from one well-studied An(IV) compound to new molecules unless they are subjected to a dedicated spectroscopic study. However, for transuranic molecules, comparison of solution and solid-state electronic absorption spectra is especially useful in providing supporting "fingerprint" evidence to correlate speciation between the bulk solid product and solution[29−31] (unlike for ^{232}Th and ^{238}U, the safety restrictions imposed to safely work with the higher specific activity ^{237}Np and ^{239}Pu radioisotopes currently preclude us from utilizing several conventional characterization techniques, such as elemental analyses and also IR spectroscopy in the case of air-sensitive compounds). Figures 2 and 3 demonstrate excellent agreement for the

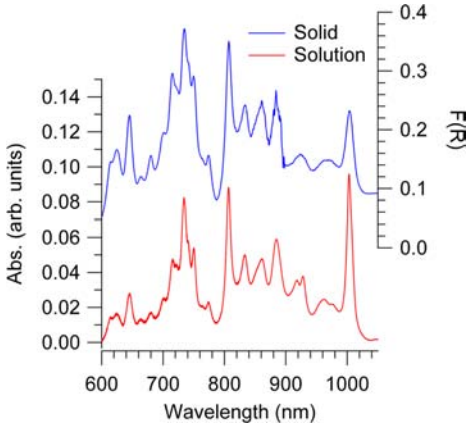

Figure 2. Vis/nIR spectrum of solid **3**, Np(^{Ar}acnac)$_4$ (top, blue), and **3** dissolved in hexanes solution (bottom, red).

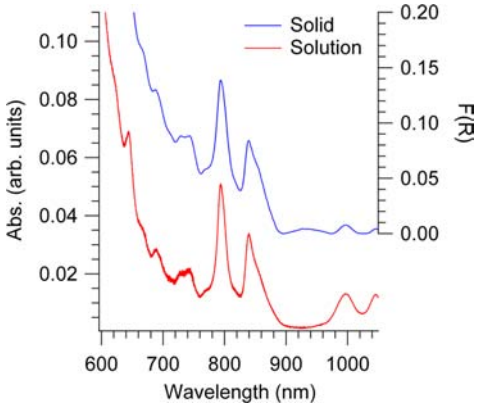

Figure 3. Vis/nIR spectrum of solid **4**, Pu(^{Ar}acnac)$_4$ (top, blue), and **4** dissolved in hexanes solution (bottom, red).

electronic transitions of **3** and **4** between the solid-state and solution spectra (compounds dissolved in hexanes). In these spectra, far more f−d and f−f transitions are observed for complex **3** (Np) than for **4** (Pu) because of masking of the lower intensity f−d and f−f bands in the visible region of the spectra by the more intense charge-transfer bands in the Pu species (separate very dilute samples were needed to resolve the charge-transfer maxima; see the Supporting Information). The electronic absorption spectra combined with the ^{1}H NMR and structural data lead to the conclusion that the An(^{Ar}acnac)$_4$ formulation found in the solid state also persists in solution.

Crystallographic analysis of complexes **1**, **2**, and **4** (Figures 4 and 5) reveals that all three complexes are isostructural and

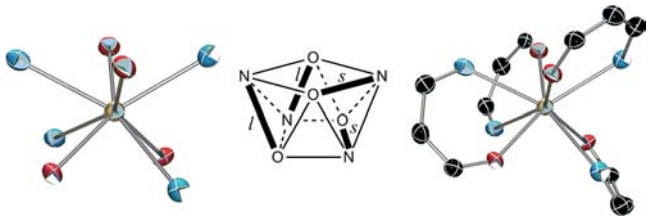

Figure 4. The primary coordination sphere around the metal center (left), ligand binding arrangement where bold bonds indicate orientation of the ^{Ar}acnac ligands (center), and ligand binding arrangement (right) of the solid-state molecular structure for Th(^{Ar}acnac)$_4$ (**1**·OC_4H_{10}·$3C_6H_{14}$) with 50% probability ellipsoids shown.

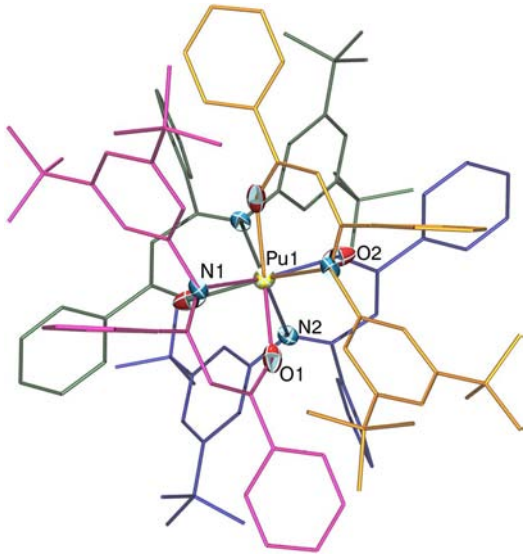

Figure 5. Solid-state molecular structure of Pu(^{Ar}acnac)$_4$ (**4**) with 50% probability ellipsoids being shown for noncarbon atoms (**1** (Th) and **2** (U) are isostructural). The individual ^{Ar}acnac ligands are color coded to better depict their arrangement.

crystallize in the monoclinic space group *C*2/*c*. The molecules consist of four ^{Ar}acnac ligands bound to the An(IV) center in a distorted square antiprismatic geometry.[32] Each square face of the primary coordination sphere consists of two nitrogen and two oxygen atoms, where the nitrogen atoms are situated at opposite corners of the square (Figure 4). The stereochemistry of the ^{Ar}acnac ligands around the metal center is best described as *ssll*, where two of the ligands are bound along the shorter (*s*) edge of a square face and the other two span the longer (*l*) edge of a triangular face (Figure 4).[33] Interestingly, this ligand arrangement is not the calculated energy minimum for a M(bidentate)$_4$ complex with square antiprismatic geometry (*llll*).[33] The stereochemistry of complexes **1**, **2**, and **4** also differs from the previously reported α-Th(acac)$_4$,[34] which adopts a dodecahedral *gggg* arrangement, as well as β-U(acac)$_4$[35] and β-Np(acac)$_4$,[36] both of which adopt square antiprismatic *ssss* stereochemistry. We believe the *ssll* ligand arrangement for complexes **1**, **2**, and **4** is required to accommodate packing of the bulky aryl groups on the ^{Ar}acnac

dx.doi.org/10.1021/ic301109f | Inorg. Chem. 2012, 51, 8557−8566

Table 1. Experimental Bond Lengths (Å) and Angles (deg) for 1, 2, and 4, and Computational Data for 1a, 2a, and 4a

	1	1a	2	2a	4	4a
An−O	2.317(3)	2.333	2.267(3)	2.240	2.177(10)	2.246
	2.324(3)	2.335	2.269(3)	2.241	2.197(8)	2.246
An−N	2.707(4)	2.706	2.676(4)	2.606	2.557(9)	2.586
	2.732(4)	2.709	2.696(4)	2.607	2.597(9)	2.587
∠N−An−O	68.2(1)	69.6	69.0(1)	71.8	70.2(3)	71.5
	69.3(1)	69.6	70.6(1)	71.7	71.9(3)	71.6

ligands, which is not a factor in the O,O donor β-diketonate acac ligand.

The isostructural nature of complexes **1**, **2**, and **4** allows for a rare direct comparison of solid-state metrical parameters going across the actinide series from Th to U, and from U to Pu (we expect that compound **3**, the Np complex, would also be isostructural, but the crystals were not of sufficient quality to allow X-ray structural determination). In complexes **1**, **2**, and **4**, there are two inequivalent An−O bonds and two inequivalent An−N bonds (the other two An−O and two An−N bonds that make up the coordination number of eight are symmetry generated by the $C2/c$ space group). Upon examination of the bond lengths when moving from Th to U (Table 1), the shortest Th−O bond in **1** is 2.317(3) Å, as compared to 2.267(3) Å for the shortest U−O bond in **2**, a shortening of 0.050 Å. The longest Th−O bond in **1** is 2.324(3) Å, while the longest U−O bond in **2** is 2.269(3) Å, a shortening of 0.055 Å. Turning to the An−N bonding, a similar comparison shows that traversing from Th to U results in a decrease of 0.031 and 0.036 Å for the shorter and longer bond lengths, respectively. The decrease in both An−O and An−N bond lengths between **1** and **2** is consistent with the actinide contraction as the ions become smaller by 0.05 Å going across the series from Th to U, resulting in a larger positive charge density at the metal center (ionic radii for 8-coordinate metal ions: Th(IV) = 1.05 Å, U(IV) = 1.00 Å).[37]

Continuing another two elements across the 5f series from **2** (U) to **4** (Pu) affords further decreases in metal−ligand bond lengths (Table 1). The shortest Pu−O bond in **4** is 2.177(10) Å, a shortening of 0.09 Å as compared to the corresponding U−O bond in **2**. The longest Pu−O bond in **4** is 2.197(8) Å, a shortening of 0.072 Å as compared to the corresponding U−O bond in **2**. Looking at the An−N bonding, a similar comparison shows that traversing from U to Pu results in a decrease of 0.119 and 0.099 Å for the shorter and longer bond lengths, respectively. The decrease observed for each bond type upon moving from U to Pu is significantly greater than the 0.04 Å difference in ionic radii when going from U to Pu (ionic radii for 8-coordinate Pu(IV) = 0.96 Å).[37]

In other series of complexes across the actinides, a trend of An−O shortening has also been observed upon moving from left to right across the periodic table. For example, in eight-coordinate $[An(\alpha_2\text{-}P_2W_{17}O_{61})_2]^{16-}$ (An = Th, U, Np, Pu, Am), the average U−O distance was shorter than the average Th−O distance by 0.048 Å.[17] In the infinite chain structure of 10-coordinate $\{C(NH_2)_3\}_4[An(C_2O_4)_4]\cdot 2H_2O$ oxalate complexes, the average U−O distance is shorter than the average Th−O distance by 0.048 and 0.031 Å, for terminal and bridging oxalate ligands, respectively.[38] For the U versus Pu comparison, in $[An(\alpha_2\text{-}P_2W_{17}O_{61})_2]^{16-}$ (An = Th, U, Np, Pu, Am), the average Pu−O distance was shorter than the average U−O distance by 0.030 Å. In the $\{C(NH_2)_3\}_4[An(C_2O_4)_4]\cdot 2H_2O$ oxalate complexes, the average Pu−O distance is shorter than the average U−O distance by 0.026 and 0.024 Å, for terminal and bridging oxalate ligands, respectively. These two literature comparisons show a smaller shortening of the An−O bonds from U(IV) to Pu(IV) as compared to that observed for **2** versus **4**. The considerable reduction in bond length from **2** to **4** is especially interesting when compared to the actinide complexes our group recently reported, $An^{IV}I_2(^{Ar}acnac)_2$ (An = U, Pu), where the An−N bond length decreases by only 0.046 Å and the An−O bonds were found to be statistically identical to each other.[19] Also intriguing is that while the average An−O bond length of **2** is 0.102 Å longer than $UI_2(^{Ar}acnac)_2$, the Pu−O bond lengths of **4** and $PuI_2(^{Ar}acnac)_2$ are identical within the 3σ criterion. One possible explanation is that the greater steric crowding in **1**−**4** that results from the binding of four $^{Ar}acnac$ ligands prevents the increased orbital interactions of the U−O bond that were calculated for the less sterically encumbered $UI_2(^{Ar}acnac)_2$ molecules, resulting in the longer U−O bond in **2**. Finally, the N−An−O bite angle of the $^{Ar}acnac$ ligand increases slightly going across the series from Th (68.2(1)° and 69.3(1)°) to Pu (70.2(3)°, 71.9(3)°), if comparing the smallest and largest values to each other, which is consistent with the decrease in An−N and An−O bond lengths. To our knowledge, there are no previous literature reports that compare isostructural Th, U, and Pu bonds to nitrogen donor atoms. This is likely a reflection of the scarcity of systematic studies across the An(IV) series, especially for anything other than oxygen-only donor ligands. Most transuranic studies are restricted to aqueous media for which oxygen donor atom ligands dominate and in which stabilization of all three elements in the tetravalent oxidation state is difficult.

Given that the $An(^{Ar}acnac)_4$ tetrakis-complexes appear to exhibit a different bonding trend across the 5f series than observed for the bis-complexes, $AnI_2(^{Ar}acnac)_2$, we sought to further understand the electronic structure and bonding properties of the tetrakis-complexes through computational modeling.

DFT calculations were performed on models for **1**, **2**, and **4** (**1a**, **2a**, and **4a**, respectively), in which the $^{Ar}acnac$ ligands have been simplified as shown in Figure 6. Key bond lengths and angles are collected in Table 1, from which it may be seen that the agreement between experiment and theory for the Th

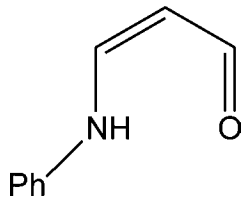

Figure 6. The simplified model for $^{Ar}acnac$ used in the computational simulations of **1a**, **2a**, and **4a**, shown with the nitrogen atom protonated.

dx.doi.org/10.1021/ic301109f | Inorg. Chem. 2012, 51, 8557−8566

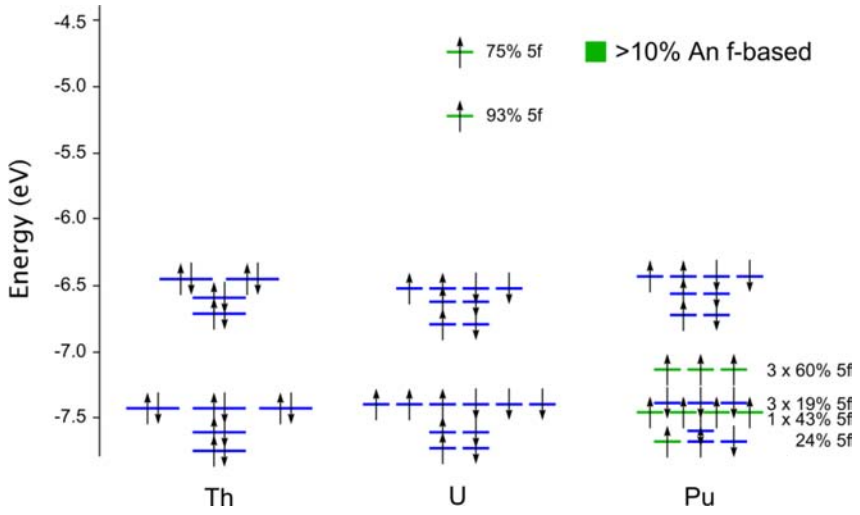

Figure 7. Valence molecular orbital energy level diagrams of **1a**, **2a**, and **4a**. Ligand-based orbitals are shown in blue, while orbitals with >10% metal 5f character are in green. The lowest energy An 6d-based orbitals are virtual in all cases (0.642, 0.616, and 0.589 eV, respectively, for **1a**, **2a**, and **4a**).

Table 2. Characteristics of the An−N and An−O Bond Critical Points for 1a, 2a, and 4a, and, in Parentheses, for 2a and 4a at the Modified Geometries Discussed in the Main Text

	An−N BCP			An−O BCP		
complex	ρ	$\nabla^2\rho$	H	ρ	$\nabla^2\rho$	H
1a	0.041	0.103	−0.002	0.073	0.267	−0.006
2a	0.047 (0.042)	0.140 (0.115)	−0.002 (−0.002)	0.088 (0.089)	0.340 (0.350)	−0.011 (−0.012)
4a	0.048 (0.047)	0.145 (0.145)	−0.002 (−0.002)	0.085 (0.098)	0.365 (0.422)	−0.009 (−0.014)

compound is excellent. For **2a** the agreement is very good for the ∠N−An−O angle, and also for r(U−O), but the calculation underestimates the U−N distance by ca. 0.07 Å. By contrast, in **4a** the situation is reversed, with essentially exact agreement for r(Pu−N), but an ca. 0.06 Å discrepancy between theory and experiment for Pu−O, with calculation overestimating this metric.

A single point energy calculation on **2a** in which the four U−N distances were set to the experimental value, with all other bond lengths and angles remaining at their optimized values, yielded a total energy only 0.36 kcal/mol less negative than that of the fully optimized structure, demonstrating that the An−N potential energy surface is very flat. For **4a**, an analogous calculation in which the four Pu−O distances were shortened to their experimental value yielded an energy 2.21 kcal/mol less negative than for the fully optimized structure, indicating that the An−O potential wells are a little steeper than the An−N around the equilibrium values, but still very shallow at 0.55 kcal/mol per Pu−O bond for this distortion. Unfortunately, a constrained geometry optimization in which the Pu−O distances were fixed to their experimental values and all other bond lengths and angles were allowed to relax (which would provide a better measure of the energy penalty for shortening r(Pu−O)) did not converge.

Valence molecular orbital energy level diagrams for **1a**, **2a**, and **4a** are shown in Figure 7. It can be seen that, in all three complexes, the energies of the highest occupied ligand-based orbitals (shown in blue) are largely unaltered from Th to Pu, while there is a very pronounced stabilization of the metal 5f-based orbitals (shown in green) from **2a** to **4a**. In the latter, the 5f-based orbitals drop below the energy of the highest occupied ligand-based levels, leading to enhanced metal/ligand orbital mixing. This has been seen many times before in actinide systems,[39−42] reflecting the stabilization and contraction of the 5f atomic orbitals as the series is crossed.

One of the traditional measures of covalency is the atomic orbital composition of MOs, with significant contributions from metal and ligand functions indicating covalency within a given MO. In the chemical community at least, covalency also carries the connotation of significant overlap between orbitals centered on different atoms, which can lead to ambiguity in the case of the middle actinides, where the energetic proximity of metal 5f and ligand orbitals can result in MOs with significant contributions from both atoms, yet little spatial overlap, resulting in the highly mixed orbital character demonstrated in **4a**. This effect is typically reflected in atomic spin densities,[42,43] where the largest deviations from formal values are found in those compounds with largest orbital mixing. In the present case, the deviations of the actinide spin density from the formal values of 2 and 4, respectively, are −0.02 for **2a** and 0.19 for **4a**, yet experience cautions against concluding that the Pu−acnac bond is more covalent than that for U (other than in a strict orbital mixing sense).

An alternative approach to assessing covalency, which we have recently begun to apply to computationally derived f-element charge densities,[41,42,44−47] is the quantum theory of atoms-in-molecules (QTAIM).[48] The QTAIM, which is also beginning to be employed experimentally in actinide chemistry,[49] tells us that there is one bond critical point (BCP) between each pair of atoms that are bonded to one another, and that chemical bonding interactions may be characterized and classified according to the properties of the BCPs; we have focused on the electron density ρ, its Laplacian $\nabla^2\rho$, and the energy density H. Values of ρ greater than 0.2 e/bohr^{-3} are typical of covalent bonds, and $\nabla^2\rho$ is generally significantly less than zero for such interactions, reflecting the

dx.doi.org/10.1021/ic301109f | Inorg. Chem. 2012, 51, 8557−8566

concentration of electron density along the bond path linking the bonded atoms. H at the BCP is negative for interactions with significant sharing of electrons, its magnitude reflecting the "covalence" of the interaction. Strongly polar bonds are characterized by low values of ρ at the BCP, together with a local charge depletion ($\nabla^2\rho > 0$).

ρ, $\nabla^2\rho$, and H for the An−N and An−O BCPs are collected in Table 2. As we have seen previously for the actinides, the data in Table 2 indicate that all of the bonds are predominantly ionic, and the metrics are all larger (in an absolute sense) for the An−O interactions, reflecting the significantly shorter bonds. The trend, in both An−N and An−O, as a function of metal is perhaps the most informative and is very much as we have seen in other actinide−ligand bonds. The electron density at the BCP increases from Th to U, and then remains approximately constant for Pu; in $AnCp_3$ and $AnCp_4$ we observed a similar pattern, with a gradual decrease from U to Cm.[41,42] The An−O energy densities also indicate that the U−O has the most covalent character, whereas for An−N all of the values are the same (and very close to zero).

The larger ionicity of the Th−ligand bonds is reflected in the natural and QTAIM atomic charges, collected in Table 3.

Table 3. Natural and, in Parentheses, QTAIM Charges of An, N, and O for 1a, 2a, and 4a

complex	An	N (av)	O (av)
1a	1.97 (2.87)	−0.56 (−1.37)	−0.74 (−1.29)
2a	1.61 (2.67)	−0.52 (−1.33)	−0.69 (−1.25)
4a	1.53 (2.60)	−0.52 (−1.34)	−0.68 (−1.25)

Clearly, the charge difference between metal and ligating atom is much larger in **1a** than **2a** and **4a** for both An−N and An−O for both sets of charge data, in keeping with the conclusions from the critical point properties. The larger negative charge on the ligand oxygen versus nitrogen atoms replicates the findings from our previous study of $AnI_2(^{Ar}acnac)_2$[19] and is in keeping with the electronegativities of the ligating atoms.

CONCLUSIONS

A series of neutral homoleptic An(IV) complexes with the ^{Ar}acnac ligand framework, $An(^{Ar}acnac)_4$ (An = Th, U, Np, Pu), have been synthesized and spectroscopically characterized, demonstrating purity and stability in both solid and organic solvent phases. The solid-state molecular structures were determined for the Th, U, and Pu complexes, offering a rare opportunity for comparison of An(IV) bonding across several actinides. Analysis of the metrical data reveals decreasing An−O and An−N bonds across the 5f series. The magnitude of these decreases appears consistent with the actinide contraction upon moving from Th to U, whereas the decreases upon moving from U to Pu are slightly larger than would be expected from the actinide contraction. Additionally, the bonding trends observed here for the tetrakis-$An(^{Ar}acnac)_4$ molecules are different from what was previously observed in the bis-$AnI_2(^{Ar}acnac)_2$ (An = U, Pu) molecules, for which an unusually short U−O bond was attributed to enhanced covalency in the U−O versus Pu−O bonding. It appears that the extra steric congestion present in the $An(^{Ar}acnac)_4$ complexes prevents these increased metal−ligand orbital interactions. The electronic structure and bonding in model $An(^{Ar}acnac)_4$ molecules was examined by DFT calculations, which reproduce the trend of shortening of both the An−O and the An−N bonds across the An(IV) series, except for the Pu−O bond, which are calculated to be slightly longer than the U−O bonds (however, the very flat energy surfaces around the An−O and An−N equilibrium values mean that the discrepancy is not of particular significance). Consideration of MO energy level diagrams shows stabilization of the 5f manifold across the An(IV) series, leading to the best energy match of 5f and ligand-based orbitals for Pu. However, poor spatial overlap suggests that this should not be interpreted as an indication of

Table 4. X-ray Crystallographic Data for Complexes $1{\cdot}OC_4H_{10}{\cdot}3C_6H_{14}$, $2{\cdot}OC_4H_{10}{\cdot}3C_6H_{14}$, and $4{\cdot}4OC_4H_8$

	$1{\cdot}OC_4H_{10}{\cdot}3C_6H_{14}$	$2{\cdot}OC_4H_{10}{\cdot}3C_6H_{14}$	$4{\cdot}4OC_4H_8$
empirical formula	$ThO_5N_4C_{138}H_{180}$	$UO_5N_4C_{138}H_{180}$	$PuO_8N_4C_{132}H_{160}$
crystal habit, color	rod, pale yellow	irregular, orange	needle, red-orange
crystal size (mm)	0.60 × 0.42 × 0.34	0.65 × 0.40 × 0.20	0.36 × 0.06 × 0.04
crystal system	monoclinic	monoclinic	monoclinic
space group	$C2/c$	$C2/c$	$C2/c$
volume (Å^3)	12 043(7)	12 081(6)	11 223(4)
a (Å)	16.120(5)	16.040(4)	15.581(3)
b (Å)	32.281(10)	32.091(9)	31.216(7)
c (Å)	23.977(8)	24.330(7)	23.872(5)
α (deg)	90	90	90
β (deg)	105.143(4)	105.271(4)	104.845(2)
γ (deg)	90	90	90
Z	4	4	4
formula weight (g/mol)	2206.90	2212.89	2169.74
density (calculated) (Mg/m^3)	1.217	1.217	1.286
absorption coefficient (mm^{-1})	1.293	1.399	0.647
F_{000}	4664	4672	4552
total no. reflections	48 386	45 825	66 741
unique reflections	11 340	10 682	12 028
final R indices [$I > 2\sigma(I)$]	R_1 = 0.0541, wR_2 = 0.1450	R_1 = 0.0448, wR_2 = 0.1296	R_1 = 0.1195, wR_2 = 0.2613
largest diff. peak and hole (e$^-$Å^{-3})	1.581 and −2.528	1.174 and −1.157	3.398 and −6.407
GOF	1.023	0.980	1.569

dx.doi.org/10.1021/ic301109f | Inorg. Chem. 2012, 51, 8557−8566

increased covalency relative to the U system. In fact, QTAIM bond critical point data indicate that all of the An−ligand bonds are predominantly ionic, with the An−O bonding containing the most covalent character and marginally greater covalency in the U and Pu systems versus the Th.

This present study, combined with our previous communication,[19] highlights how relatively small changes in chemical speciation (bis- versus tetrakis-^{Ar}acnac complexes, which vary in the number of coordinated ^{Ar}acnac ligands and presence/lack of coordinated halide anions) can cause different bonding trends across the actinide series, reflecting the complicated nature of actinide ion interactions with ligands that have the potential to engage in covalent bonding contributions. Therefore, it is important that more isostructural comparisons across several actinide metals are pursued in the future to gain a better comprehension of chemical and electronic differences that may ultimately find exploitation in the design of new separation processes for the nuclear industry and waste disposition/cleanup options.

EXPERIMENTAL SECTION

General Information for Thorium and Uranium Experimentation. All thorium and uranium reactions and subsequent manipulations were performed under anaerobic and anhydrous conditions under either high vacuum or an atmosphere of nitrogen or argon. THF, hexanes, diethyl ether, and toluene were dried using a Vacuum Atmospheres DRI-SOLV solvent purification system. C_6H_6 and C_6D_6 were dried over activated 4 Å molecular sieves for 24 h before use, while CH_2Cl_2 and CD_2Cl_2 were dried over activated 3 Å molecular sieves for 24 h before use. $ThCl_4(DME)_2$[50] and UCl_4[51,52] were synthesized according to previously published procedures. H(^{Ar}acnac) (Ar = 3,5-^{t}Bu$_2$C$_6$H$_3$) was also synthesized according to previously reported procedures,[53] while all other reagents were purchased from commercial suppliers and used as received.

The ^{1}H COSY NMR spectrum for **2** was obtained using a Varian Unity Inova AS600 600 MHz spectrometer. All additional NMR spectra were recorded on a Varian UNITY INOVA 400 MHz or Varian UNITY INOVA 500 MHz spectrometer. ^{1}H NMR spectra were referenced to $SiMe_4$ using the residual protio solvent peaks as an internal standard.[54] IR spectra were recorded on a Mattson Genesis FTIR spectrometer, while UV/vis/NIR experiments were performed on a UV-3600 Shimadzu spectrophotometer. Elemental analyses were performed by the Microanalytical Laboratory at UC Berkeley.

The solid-state molecular structures of complexes **1** and **2** were determined (see Table 4) as follows. Crystals were mounted on a glass fiber under Paratone-N oil. Data collection was carried out a Bruker 3-axis platform diffractometer with SMART-1000 CCD detector. The instrument was equipped with graphite monochromatized Mo Kα X-ray source (λ = 0.71073 Å). All data were collected at 150(2) K using an Oxford nitrogen gas cryostream system. A hemisphere of data was collected using ω scans and 0.3° frame widths. Frame exposures of 10 and 15 s were used for **1** and **2**, respectively. SMART was used to determine the cell parameters, and the raw frame data were processed using SAINT.[55,56] The empirical absorption correction was applied on the basis of SADABS. Subsequent calculations were carried out using SHELXTL.[57] Structures were solved using direct methods and difference Fourier techniques. All hydrogen atom positions were idealized, and rode on the atom of attachment, while the final refinement included anisotropic temperature factors on all non-hydrogen atoms unless otherwise mentioned. Structure solution, refinement, graphics, and creation of publication materials were performed using SHELXTL.

Both complexes **1** and **2** contained badly disordered solvents of crystallization. In the case of **1**, the electron density due to disordered hexane and Et_2O was removed with the SQUEEZE program.[58] In the case of **2**, the Et_2O solvate molecule was successfully refined; however, the hexane solvate could not be refined. As a result, it was also removed using the SQUEEZE program.

General Information for Transuranic Experimentation. All neptunium and plutonium reactions were performed with ^{237}Np and ^{239}Pu isotopes obtained internally from Los Alamos National Laboratory. This work was conducted inside a radiological facility approved and regulated for the handling and manipulation of high specific-activity α-emitting radionuclides. Reactions were performed inside a negative pressure helium atmosphere drybox (MBraun Labmaster 130). Solvents were purchased in anhydrous grade and stored over a 1:1 mixture of dried 3 and 4 Å molecular sieves inside the drybox prior to use. The preparations of $[PPh_4]_2[NpCl_6]$ and $[PPh_4]_2[PuCl_6]$ (utilized as starting materials for the transuranic reactions) are described elsewhere.[18] ^{1}H NMR spectra of Np and Pu containing samples were measured inside 4 mm PTFE NMR tube liners placed inside 5 mm glass NMR tubes, to satisfy multiple containment local safety requirements. NMR spectra were recorded on a Bruker Avance 300 MHz spectrometer, and referenced to residual solvent protio resonances. Electronic absorption spectra were recorded on Varian Cary 6000i (solution) and Cary 500 (solid) UV/vis/NIR spectrophotometers.

A Pu containing single crystal of **4** was coated in paratone-N oil and mounted inside a 0.5 mm capillary tube, which was sealed with hot capillary wax. After removal from the drybox, the capillary was coated with a thin film of acrylic in ethyl acetate (Hard as Nails) to provide structural integrity and additional containment. The capillary was placed on a Bruker Platform diffractometer with 1k CCD, and cooled to 141(2) K using a Bruker Kryoflex cryostat (see Table 4 for crystallographic data). The instrument was equipped with a sealed, graphite monochromatized Mo Kα X-ray source (λ = 0.71073 Å). A hemisphere of data was collected using ω scans, with 30 s frame exposures and 0.3° frame widths. Data collection and initial indexing and cell refinement were handled using SMART software.[59] Frame integration, including Lorentz-polarization corrections, and final cell parameter calculations were carried out using SAINT software.[60] The data were corrected for absorption using the SADABS program.[61] Decay of reflection intensity was monitored via analysis of redundant frames. The structure was solved using direct methods and difference Fourier techniques. Hydrogen atoms were idealized. The final refinement included anisotropic temperature factors on all non-hydrogen atoms. The crystal was composed of many twin domains, and attempts to index and integrate twin components were not successful. The major component was indexed and integrated, and the structure solution and refinement yielded the correct structure. The 46 worst offending reflections, with $F_o \gg F^c$, were omitted from the refinement. Structure solution, refinement, and materials for publication were performed using SHELXTL.[62] The electron density due to disordered lattice THF was removed with the SQUEEZE program.[58]

Despite numerous attempts with single crystals of high quality to the naked eye, we were unable to obtain X-ray diffraction data of sufficient quality to allow structural determination of **3**, the Np-containing complex.

Th(^{Ar}acnac)$_4$ (1). To an Et_2O (3 mL) suspension of $ThCl_4(DME)_2$ (50.8 mg, 0.092 mmol) was added an orange Et_2O (4 mL) solution containing 4 equiv of Na(^{Ar}acnac), produced in situ using an equimolar ratio of H(^{Ar}acnac) (151.5 mg, 0.368 mmol) and $Na[N(SiMe_3)_2]$ (67.4 mg, 0.368 mmol). Stirring for 17 h resulted in the formation of a yellow solution and a pale colored solid. The solution was filtered through a Celite column supported on glass wool (0.5 cm × 2 cm) and concentrated in vacuo (2 mL), resulting in the deposition of a yellow microcrystalline material. Addition of acetonitrile (6 mL) and storage at −25 °C for 3 h produced additional yellow microcrystalline solid. The supernatant was decanted off, and the solid was rinsed with acetonitrile (2 × 2 mL) before being dried in vacuo (116.2 mg, 68% yield). Single crystals suitable for X-ray diffraction were grown from a mixture of Et_2O and hexanes (Table 4). Anal. Calcd for $ThO_4N_4C_{116}H_{128}$: C, 74.33; H, 6.88; N, 2.99. Found: C, 73.94; H, 6.88; N, 2.94. ^{1}H NMR (CD_2Cl_2, 25 °C, 500 MHz): δ 7.53 (d, 8H, J_{HH} = 7.5 Hz, ortho CH), 7.22 (t, 4H, J_{HH} = 7.2 Hz, para

dx.doi.org/10.1021/ic301109f | Inorg. Chem. 2012, 51, 8557−8566

CH), 7.15 (t, 8H, J_{HH} = 7.5 Hz, meta CH), 6.87 (s, 20H, overlapping ortho, meta, and para CH), 6.69 (s, 4H, para ArCH), 6.26 (s, 4H, ortho ArCH), 6.23 (s, 4H, ortho ArCH), 5.95 (s, 4H, γ-CH), 0.87 (s, 36H, CMe_3), 0.70 (s, 36H, CMe_3). IR (KBr pellet, cm^{-1}): 3082(w), 3060(w), 3034(w), 2962(vs), 2952(vs), 2928(sh m), 2902(m), 2866(m), 1591(vs), 1566(vs), 1499(sh vs), 1486(vs), 1472(vs), 1460(vs), 1400(s), 1424(s), 1401(vs), 1393(sh vs), 1361(s), 1292(s), 1278(sh s), 1246(m), 1234(sh m), 1202(w), 1182(w), 1157(w), 1134(w), 1127(sh w), 1103(w), 1076(sh m), 1063(s), 1025(m), 1001(w), 981(w), 973(sh w), 953(w), 923(w), 911(sh w), 897(m), 890(m), 869(m), 841(w), 820(w), 801(w), 782(w), 768(s), 761(s), 725(sh w), 712(sh m), 704(sh s), 696(s), 676(w), 663(w), 650(sh w), 618(sh w), 607(m), 576(m), 569(m), 548(w), 523(w), 499(m), 482(sh w), 458(sh w), 452(w), 440(w), 428(sh w).

*U(^{Ar}acnac)$_4$ (**2**).* To a vial containing UCl_4 (59.4 mg, 0.156 mmol) was added an orange Et_2O (5 mL) solution containing 4 equiv of Na(^{Ar}acnac) produced in situ using an equimolar ratio of H(^{Ar}acnac) (257.9 mg, 0.627 mmol) and $Na[N(SiMe_3)_2]$ (114.0 mg, 0.622 mmol). Stirring for 18 h resulted in the formation of a burnt-orange solution and an orange colored solid. The volatiles were removed in vacuo, and hexane (2 mL) was added and removed in vacuo to ensure all of the Et_2O had been eliminated. Hexane (10 mL) was again added to the solution, resulting in a dark burnt orange solution and an orange solid. The solution was filtered through a Celite column supported on glass wool (0.5 cm × 2 cm), and the volatiles were removed from the filtrate in vacuo. The resulting solid was dissolved in Et_2O (2 mL), producing a dark burnt orange solution. The solution was filtered again through a Celite column supported on glass wool (0.5 cm × 2 cm). Subsequent addition of acetonitrile (6 mL) resulted in the deposition of burnt orange microcrystalline material. Storage at −25 °C for 5 days resulted in further deposition of burnt orange microcrystalline solid. The supernatant was decanted off and the solid was rinsed with acetonitrile (3 × 3 mL) before being dried in vacuo (189.3 mg, 64% yield). Single crystals suitable for X-ray diffraction were grown from a mixture of Et_2O and hexane. Anal. Calcd for $UO_4N_4C_{116}H_{128}$: C, 74.10; H, 6.86; N, 2.98. Found: C, 73.78; H, 6.78; N, 2.92. ^{1}H NMR (CD_2Cl_2, 25 °C, 500 MHz): δ 19.07 (s, 4H, ortho ArCH), 18.98 (br s, 8H, ortho CH), 10.40 (t, 4H, J_{HH} = 6.8 Hz, para CH), 10.14 (s, 8H, meta CH), 6.26 (t, 4H, J_{HH} = 7.5 Hz, para CH), 5.89 (s, 4H, para ArCH), 5.72 (s, 4H, γ-CH), 5.58 (br s, 8H, meta CH), 3.61 (s, 36H, CMe_3), −2.76 (s, 36H, CMe_3), −23.24 (s, 4H, ortho ArCH). The resonance corresponding to the ortho protons on one of the phenyl rings is not observed, possibly due to paramagnetic broadening. IR (KBr pellet, cm^{-1}): 3077(w), 3060(w), 3032(w), 2961(s), 2952(s), 2922(sh m), 2901(m), 2866(m), 1589(vs), 1562(vs), 1536(w), 1498(sh vs), 1489(vs), 1485(vs), 1472(sh vs), 1457(sh vs), 1440(s), 1425(s), 1396(vs), 1361(s), 1341(w), 1292(s), 1245(m), 1241(sh m), 1203(w), 1182(w), 1157(w), 1133(w), 1128(w), 1102(w), 1075(sh m), 1063(s), 1025(m), 1001(w), 982(w), 970(sh w), 954(w), 934(sh w), 923(w), 911(sh w), 896(m), 889(m), 870(m), 839(w), 820(w), 800(w), 782(m), 767(s), 765(s), 728(sh w), 704(sh s), 696(vs), 666(m), 650(sh w), 619(sh w), 607(m), 576(s), 568(sh m), 547(m), 524(m), 499(m), 491(sh m), 481(m), 457(m), 437(m), 431(sh m), 413(m). UV/vis/NIR (CH_2Cl_2, 2.75 × 10^{-3} M, L mol^{-1} cm^{-1}): 568 nm (ε = 223), 612 nm (ε = 121), 656 nm (ε = 92), 690 nm (ε = 133), 796 nm (ε = 11), 860 nm (sh, ε = 12), 900 nm (ε = 19), 1020 nm (ε = 41), 1054 nm (ε = 45), 1098 nm (sh, ε = 51), 1122 nm (ε = 55), 1162 nm (sh, ε = 32), 1256 nm (ε = 14), 1434 nm (ε = 48), 1484 nm (ε = 52), 1610 nm (ε = 14), 1662 nm (ε = 14), 1862 nm (ε = 3), 2004 nm (sh, ε = 8), 2176 nm (ε = 42).

*Np(^{Ar}acnac)$_4$ (**3**).* To a vial containing solid $[PPh_4]_2[NpCl_6]$ (0.0217 g, 0.019 mmol) was added an orange solution of H^{Ar}acnac (0.0317 g, 0.077 mmol) and $Na[N(SiMe_3)_2]$ (0.0141 g, 0.077 mmol) in THF (3 mL). The mixture was heated at 50 °C for 1 h during which time a pronounced color change to deep orange occurred. This cloudy orange solution was then stirred at room temperature for 14 h. The solution was filtered through Celite to afford a clear deep orange solution. The solvent was removed in vacuo from the filtrate. Hexanes (4 mL) was added to the residue with heating at 40 °C for 20 min. The resulting orange solution was filtered through a glass fiber filter circle, and the solvent was removed in vacuo. The residue was dissolved in THF (1 mL), 3−4 drops of MeCN were carefully added, and the solution was stored at −35 °C. After 1 d the first crop of orange crystalline solid (square/rectangular plates) was collected, and a second crop was collected after 4 d. The two crops were combined and dried in vacuo (0.0170 g, 47% yield). Solid-state diffuse reflectance UV/vis/nIR in nm: 615, 625, 645, 664, 680, 702, 716, 735, 750, 774, 807, 834, 861, 884, 924, 963, 973, 1004. UV/vis/nIR of **3** dissolved in hexanes solution in nm, 8.18 × 10^{-4} M (ε, L mol^{-1} cm^{-1}): 615 (18), 625 (20), 645 (34), 664 (16), 680 (21), 701 (31), 716 (58), 734 (101), 750 (66), 774 (29), 807 (108), 833 (61), 861 (58), 885 (72), 918 (44), 928 (46), 962 (30), 975 (27), 1003 (117).

UV/vis/nIR of **3** dissolved in hexanes solution and diluted to observe charge-transfer bands, in nm, 9.69 × 10^{-6} M (ε, L mol^{-1} cm^{-1}): 251 (41 067), 368 (32 872).

^{1}H NMR (CD_2Cl_2, 25 °C, 300 MHz): δ 9.54 (br s, 8H, ortho CH), 8.15 (t, 4H, J_{HH} = 7.1 Hz, para CH), 7.56 (br s, 8H, meta CH), 6.85 (t, 4H, J_{HH} = 7.2 Hz, para CH), 6.72 (br s, 8H, ortho CH), 6.59 (br s, 8H, meta CH), 5.72 (s, 4H, γ-CH), 5.41 (br s, 4H, ortho ArCH), 4.63 (s, 4H, para ArCH), 1.06 (br s, 4H, ortho ArCH), 0.75 (s, 36H, CMe_3), 0.38 (s, 36H, CMe_3).

*Pu(^{Ar}acnac)$_4$ (**4**).* To a vial containing solid $[PPh_4]_2[PuCl_6]$ (0.0185 g, 0.016 mmol) was added an orange solution of H^{Ar}acnac (0.0269 g, 0.065 mmol) and $Na[N(SiMe_3)_2]$ (0.0120 g, 0.065 mmol) in THF (3 mL). The mixture was heated at 50 °C for 40 min during which time a cloudy deep red solution formed. Stirring was continued at room temperature for 14 h. The solution was filtered through Celite to afford a clear deep red solution. The solvent was removed in vacuo from the filtrate. Hexanes (2 mL) was added to the residue with heating at 40 °C for 10 min. The resulting red solution was filtered through a glass fiber filter circle, and the solvent was removed in vacuo. The residue was dissolved in THF (1 mL), 3−4 drops of MeCN were carefully added, and the solution was stored at −35 °C. After 2 d the red crystalline solid (square/rectangular plates) was collected and dried in vacuo (0.0181 g, 59% yield). A crystal suitable for X-ray diffraction structural determination was taken grown from the same solution conditions as the bulk product. Crystals appeared orange-red under the microscope light.

Solid-state diffuse reflectance UV/vis/nIR in nm: 688, 729, 742, 794, 839, 996, 1047.

UV/vis/nIR of **4** dissolved in hexanes solution in nm, 3.21 × 10^{-4} M (ε, L mol^{-1} cm^{-1}): 645 (215), 689 (90), 728 (63), 742 (67), 793 (158), 840 (106), 997 (41), 1046 (40).

UV/vis/nIR of **4** dissolved in hexanes solution and diluted to observe charge-transfer bands, in nm, 1.57 × 10^{-5} M (ε, L mol^{-1} cm^{-1}): 249 (65 414), 352 (53 519).

^{1}H NMR (CD_2Cl_2, 25 °C, 300 MHz): δ 14.14 (s, 4H, ortho ArCH), 7.59 (very br s, ortho CH), 7.13 (br s, 12H, overlapping para CH and ortho CH), 6.67 (s, 4H, J_{HH} = 7.2 Hz, para CH), 6.28 (t, 8H, J_{HH} = 7.7 Hz, meta CH), 6.13 (s, 4H, para ArCH), 5.96 (s, 4H, γ-CH), 4.58 (br s, 8H, meta CH), 1.89 (s, 36H, CMe_3), 0.96 (br s, 4H, ortho ArCH), −0.26 (s, 36H, CMe_3).

Computational Details. Geometry optimizations were performed on **1a**, **2a**, and **4a** using the Amsterdam Density Functional code version 2010.02,[63,64] with the PBE0 functional and Slater Type Orbital basis sets of TZP quality for the actinides and DZP quality for all other atoms.[65] Frozen atomic cores up to 5d for the actinides and 1s for second period atoms were employed. Relativistic effects were included via the scalar zeroth-order regular approximation to the Dirac equation. Fermi smearing across 0.002 au was used to aid convergence of the SCF without creating fractional occupations in the final structure. The integration parameter was increased to 4.5 for improved accuracy.

Single-point calculations were performed at the ADF geometries with the Gaussian 09 (revision A.02) code,[66] using the segmented all-electron relativistic basis sets with polarization functions (SARCP) for the actinides,[67] and the standard Pople 6-31G** basis sets for other atoms, with the "ultrafine" integration grid setting to allow sufficient accuracy for the high orbital curvature in the actinide nuclear regions.

dx.doi.org/10.1021/ic301109f | Inorg. Chem. 2012, 51, 8557−8566

Point charge nuclei were used, as recommended for the SARCP basis set, rather than the default Gaussian form. Relativistic effects were included by using the spin−orbit-free Douglas−Kroll−Hess Hamiltonian. The resulting wave function files were then used as input to the AIMAll package for QTAIM analysis.[68]

■ ASSOCIATED CONTENT

Supporting Information

Additional figures and tables, as well as CIF data. Complete ref 66. This material is available free of charge via the Internet at http://pubs.acs.org.

■ AUTHOR INFORMATION

Corresponding Author

*E-mail: gaunt@lanl.gov (A.J.G.), hayton@chem.ucsb.edu (T.W.H.), n.kaltsoyannis@ucl.ac.uk (N.K.).

Notes

The authors declare no competing financial interest.

■ ACKNOWLEDGMENTS

We are grateful to the University of California, Santa Barbara, and the University of California Laboratory Fees Program for support. A.J.G., S.D.R., and M.B.J. thank the U.S. Department of Energy, Office of Science, Early Career Research Program (contract DE-AC52-06NA25396). D.D.S. thanks the Seaborg Institute Summer Research Fellowship Program at Los Alamos National Laboratory. We are grateful to the U.K.'s Nuclear Decommissioning Authority for a Ph.D. studentship to I.K., and for providing industrial supervision via the National Nuclear Laboratory. We thank the EPSRC for computing resources under grant GR/S06233 and via its National Service for Computational Chemistry Software (http://www.nsccs.ac.uk). We also thank UCL for computing resources via the Research Computing "Legion" cluster and associated services.

■ REFERENCES

(1) *The Chemistry of the Actinide and Transactinide Elements*, 3rd ed.; Morss, L. R., Edelstein, N. M., Fuger, J., Katz, J. J., Eds.; Springer: Dordrecht, The Netherlands, 2006.

(2) (a) Spent Fuel Reprocessing Options, IAEA-TECDOC-1587, August 2008, http://www-pub.iaea.org/MTCD/publications/PDF/te_1587_web.pdf. (b) Nuclear Energy Advisory Committee Report, November 2008, commissioned by the U.S. Department of Energy, http://www.ne.doe.gov/neac/neacPDFs/NEAC_Final_Report_Web%20Version.pdf. (c) Basic Research Needs for Advanced Nuclear Energy Systems, Report of the Basic Energy Sciences Workshop on Basic Research Needs for Advanced Nuclear Energy Systems, July 31−August 1, 2006, http://www.sc.doe.gov/bes/reports/files/ANES_rpt.pdf.

(3) Gaunt, A. J.; Neu, M. P. *C. R. Chim.* **2010**, *13*, 821.

(4) Ephritikhine, M. *Dalton Trans.* **2006**, 2501.

(5) Wigeland, R. A.; Bauer, T. H.; Fanning, T. H.; Morris, E. E. *Nucl. Technol.* **2006**, *154*, 95.

(6) Choppin, G. R. *J. Alloys Compd.* **2002**, *344*, 55.

(7) Brennan, J. G.; Stults, S. D.; Andersen, R. A.; Zalkin, A. *Organometallics* **1988**, *7*, 1329.

(8) Jensen, M. P.; Bond, A. H. *J. Am. Chem. Soc.* **2002**, *124*, 9870.

(9) Roger, M.; Barros, N.; Arliguie, T.; Thuéry, P.; Maron, L.; Ephritikhine, M. *J. Am. Chem. Soc.* **2006**, *128*, 8790.

(10) Kolarik, Z. *Chem. Rev.* **2008**, *108*, 4208.

(11) Ekberg, C.; Fermvik, A.; Retegan, T.; Skarnemark, G.; Foreman, M. R. S.; Hudson, M. J.; Englund, S.; Nilsson, M. *Radiochim. Acta* **2008**, *96*, 225.

(12) Lewis, F. W.; Harwood, L. M.; Hudson, M. J.; Drew, M. G. B.; Desreux, J. F.; Vidick, G.; Bouslimani, N.; Modolo, G.; Wilden, A.; Sypula, M.; Vu, T.-H.; Simonin, J.-P. *J. Am. Chem. Soc.* **2011**, *133*, 13093.

(13) Aneheim., E.; Ekberg, C.; Fermvik, A.; Foreman, M. R. S. J.; Retegan, T.; Skarnemark, G. *Solvent Extr. Ion Exch.* **2010**, *28*, 437.

(14) Diamond, R. M.; Street, K., Jr.; Seaborg, G. T. *J. Am. Chem. Soc.* **1954**, *76*, 1461.

(15) Minasian, S. G.; Krinsky, J. L.; Arnold, J. *Chem.-Eur. J.* **2011**, *17*, 12234.

(16) Gaunt, A. J.; Reilly, S. D.; Enriquez, A. E.; Scott, B. L.; Ibers, J. A.; Sekar, P.; Ingram, K. I. M.; Kaltsoyannis, N.; Neu, M. P. *Inorg. Chem.* **2008**, *47*, 29 and references therein.

(17) Sokolova, M. N.; Fedosseev, A. M.; Andreev, G. B.; Budantseva, N. A.; Yusov, A. B.; Moisy, P. *Inorg. Chem.* **2009**, *48*, 9185.

(18) Minasian, S. G.; Boland, K. S.; Feller, R. K.; Gaunt, A. J.; Kozimor, S. A.; May, I.; Reilly, S. D.; Scott, B. L.; Shuh, D. K. *Inorg. Chem.* **2012**, *51*, 5728 and references therein.

(19) Schnaars, D. D.; Batista, E. R.; Gaunt, A. J.; Hayton, T. W.; May, I.; Reilly, S. D.; Scott, B. L.; Wu, G. *Chem. Commun.* **2011**, *47*, 7647.

(20) Schnaars, D. D.; Wu, G.; Hayton, T. W. *Inorg. Chem.* **2011**, *50*, 4695.

(21) Schnaars, D. D.; Wu, G.; Hayton, T. W. *Inorg. Chem.* **2011**, *50*, 9642.

(22) Liu, G.; Beitz, J. V. In *The Chemistry of the Actinide and Transactinide Elements*, 3rd ed.; Morss, L. R., Edelstein, N. M., Fuger, J., Katz, J. J., Eds.; Springer: Doredrecht, The Netherlands, 2006; Vol. 3, pp 2013−2111.

(23) Carnall, W. T.; Liu, G. K.; Williams, C. W.; Reid, M. F. *J. Chem. Phys.* **1991**, *95*, 7194.

(24) Krupa, J. C. *Inorg. Chim. Acta* **1987**, *139*, 223.

(25) Ryan, J. L.; Jørgensen, C. K. *Mol. Phys.* **1963**, *7*, 17.

(26) Kraus, K. A.; Nelson, F. *J. Am. Chem. Soc.* **1950**, *72*, 3901.

(27) Hagan, P. G.; Cleveland, J. M. *J. Inorg. Nucl. Chem.* **1966**, *28*, 2905.

(28) Cohen, D. *J. Inorg. Nucl. Chem.* **1961**, *18*, 211.

(29) Gaunt, A. J.; May, I.; Neu, M. P.; Reilly, S. D.; Scott, B. L. *Inorg. Chem.* **2011**, *50*, 4244.

(30) Berthon, C.; Boubals, N.; Charushnikova, I. A.; Collison, D.; Cornet, S. M.; Den Auwer, C.; Gaunt, A. J.; Kaltsoyannis, N.; May, I.; Petit, S.; Redmond, M. P.; Reilly, S. D.; Scott, B. L. *Inorg. Chem.* **2010**, *49*, 9554.

(31) Gaunt, A. J.; Reilly, S. D.; Hayton, T. W.; Scott, B. L.; Neu, M. P. *Chem. Commun.* **2007**, 1659.

(32) Haigh, C. W. *Polyhedron* **1995**, *14*, 2871.

(33) Hay, B. P.; Uddin, J.; Firman, T. K. *Polyhedron* **2004**, *23*, 145.

(34) Allard, B. *Acta Chem. Scand.* **1976**, *A 30*, 461.

(35) Titze, H. *Acta Chem. Scand.* **1970**, *24*, 405.

(36) Allard, B. *Acta Chem. Scand.* **1972**, *26*, 3492.

(37) Shannon, R. D. *Acta Crystallogr.* **1976**, *A 32*, 751.

(38) Andreev, G.; Budantseva, N.; Fedoseev, A.; Moisy, P. *Inorg. Chem.* **2011**, *50*, 11481.

(39) Strittmatter, R. J.; Bursten, B. E. *J. Am. Chem. Soc.* **1991**, *113*, 552.

(40) Ingram, K. I. M.; Tassell, M. J.; Gaunt, A. J.; Kaltsoyannis, N. *Inorg. Chem.* **2008**, *47*, 7824.

(41) Tassell, M. J.; Kaltsoyannis, N. *Dalton Trans.* **2010**, *39*, 6719.

(42) Kirker, I.; Kaltsoyannis, N. *Dalton Trans.* **2011**, *40*, 124.

(43) Prodan, I. D.; Scuseria, G. E.; Martin, R. L. *Phys. Rev. B* **2007**, *76*, 033101.

(44) Arnold, P. L.; Turner, Z. R.; Kaltsoyannis, N.; Pelekanaki, P.; Bellabarba, R. M.; Tooze, R. B. *Chem.-Eur. J.* **2010**, *16*, 9623.

(45) Saleh, L. M. A.; Birjkumar, K. H.; Protchenko, A. V.; Schwarz, A. D.; Aldridge, S.; Jones, C.; Kaltsoyannis, N.; Mountford, P. *J. Am. Chem. Soc.* **2011**, *133*, 3836.

(46) Mansell, S. M.; Kaltsoyannis, N.; Arnold, P. L. *J. Am. Chem. Soc.* **2011**, *133*, 9036.

(47) Blake, M. P.; Kaltsoyannis, N.; Mountford, P. *J. Am. Chem. Soc.* **2011**, *133*, 15358.

(48) Bader, F. *Atoms in Molecules: A Quantum Theory*; OUP: Oxford, 1990.

(49) Zhurov, V. V.; Zhurova, E. A.; Pinkerton, A. A. *Inorg. Chem.* **2011**, *50*, 6330.
(50) Cantat, T.; Scott, B. L.; Kiplinger, J. L. *Chem. Commun.* **2010**, *46*, 919.
(51) Kiplinger, J. L.; Morris, D. E.; Scott, B. L.; Burns, C. J. *Organometallics* **2002**, *21*, 5978.
(52) Hermann, J. A.; Suttle, J. F.; Hoekstra, H. R. *Inorg. Synth.* **1957**, *5*, 143.
(53) Hayton, T. W.; Wu, G. *Inorg. Chem.* **2009**, *48*, 3065.
(54) Fulmer, G. R.; Miller, A. J. M.; Sherden, N. H.; Gottlieb, H. E.; Nudelman, A.; Stoltz, B. M.; Bercaw, J. E.; Goldberg, K. I. *Organometallics* **2010**, *29*, 2176.
(55) *SMART Software Users Guide*, 5.1 ed.; Bruker Analytical X-ray Systems Inc.: Madison, WI, 1999.
(56) *SAINT Software Users Guide*, 5.1 ed.; Bruker Analytical X-ray Systems Inc.: Madison, WI, 1999.
(57) Sheldrick, G. M. *SHELXTL*, 6.12 ed.; Bruker Analytical X-ray Systems Inc.: Madison, WI, 2001.
(58) Spek, A. L. *J. Appl. Crystallogr.* **2003**, *36*, 7.
(59) *SMART 5.632*; Bruker AXS, Inc.: Madison, WI, 2005.
(60) *SAINT+ 6.45*; Bruker AXS, Inc.: Madison, WI, 2003.
(61) Sheldrick, G. M. *SADABS 2.05*; University of Göttingen: Germany, 2002.
(62) *SHELXTL Version 6.10*; Bruker AXS, Inc.: Madison, WI, 2001.
(63) Fonseca Guerra, C.; Snijders, J. G.; te Velde, G.; Baerends, E. J. *Theor. Chem. Acc.* **1998**, *99*, 391.
(64) te Velde, G.; Bickelhaupt, F. M.; Van Gisbergen, S.; Fonseca Guerra, C.; Baerends, E. J.; Snijders, J. G.; Ziegler, T. *J. Comput. Chem.* **2001**, *22*, 931.
(65) Adamo, C.; Barone, V. *J. Chem. Phys.* **1999**, *110*, 6158.
(66) Frisch, M. J.; et al. *Gaussian 09*, revision A.02; Gaussian, Inc.: Wallingford, CT, 2009. See the Supporting Information for a full author list.
(67) Pantazis, D. A.; Neese, F. *J. Chem. Theory Comput.* **2011**, *7*, 677.
(68) Keith, T. A. *AIMAll 11.10.16*; TK Gristmill Software: 2011.